Published in final edited form as:
Adv Chronic Kidney Dis. 2013 November ; 20(6): 466–478. doi:10.1053/j.ackd.2013.08.004.

Perfluorocarbon Nanoparticles for Physiological and Molecular Imaging and Therapy

Junjie Chen, **Hua Pan**, **Gregory M. Lanza**, and **Samuel A. Wickline***
Departments of Medicine Washington University in St. Louis, MO, 63130, USA

Abstract

Herein we review the use of non-nephrotoxic perfluorocarbon nanoparticles (PFC NP) for noninvasive detection and therapy of kidney diseases, and provide a synopsis of other related literature pertinent to anticipated clinical application. Recent reports indicate that PFC NP allow quantitative mapping of kidney perfusion, and oxygenation after ischemia-reperfusion injury with the use of a novel multi-nuclear $^{1}H/^{19}F$ magnetic resonance imaging (MRI) approach,. Furthermore, when conjugated with targeting ligands, the functionalized PFC NP offer unique and quantitative capabilities for imaging inflammation in the kidney of atherosclerotic ApoE-null mice. Additionally, PFC NP can facilitate drug delivery for treatment of inflammation, thrombosis, and angiogenesis in selected conditions that are comorbidities for to kidney failure. The excellent safety profile of PFC NP with respect to kidney injury positions these nanomedicine approaches as promising diagnostic and therapeutic candidates for treating and following acute and chronic kidney diseases.

Keywords

Nanoparticles; Molecular Imaging; Perfluorocarbon; Perfusion; Oxygenation

A. Introduction

In this brief review, we introduce the topic of nanomedicine approaches for detection and potential therapy of acute and chronic kidney diseases. The prevalence and severe consequences of ischemia, hypoperfusion, and hypoxia on renal function mark these pathological substrates as clear targets for new approaches to ameliorate or preserve kidney function, especially in acute kidney injury where diagnosis is challenging and therapy primarily supportive. Because the kidney is a highly metabolic organ, protracted bouts of

*Send correspondence to: Samuel A. Wickline, MD, C-TRAIN Group, Campus Box 8215, Washington University School of Medicine, St. Louis, MO 63108, USA, Phone: 314-454-8635, Fax: 314-454-5265, saw@wuphysics.wustl.edu.

Financial Disclosure:
Wickline, SA: equity in Kereos, Inc.
Lanza, GM: equity in Kereos, Inc.

ischemia or hypoxia can initiate an injury program leading to extensive cellular necrosis and/or apoptosis, especially under circumstances of mixed acute and chronic disease, or in the face of comorbidities such as diabetes or atherosclerosis or sepsis. Accordingly, sensitive noninvasive methods to detect and monitor intrarenal blood flow and tissue oxygenation could be a boon to emerging therapeutic regimens designed more specifically to interdict the progression of renal dysfunction at its earliest stages.

Unfortunately, quantitative methods for assessing kidney hypoxia are neither well developed nor commonly deployed in the clinic. Traditional blood and urine markers, such GFR or kidney injury molecules, do not provide direct measures of kidney hypoxic injury. Even such metrics as total oxygen consumption based on the difference in arterial and venous pO_2 appears insensitive to kidney hypoxia because less than 10% of delivered oxygen is needed for kidney metabolism.[1] Although contrast-enhanced CT or MRI could provide multiple indexes (e.g. time of peak perfusion, blood volume) for assessing kidney perfusion,[2–4] the increased risk of contrast agent induced kidney failure or nephrogenic systemic fibrosis limits the application of these imaging methods for patients with existing kidney diseases.[5–8]

In the last two decades, non-invasive BOLD and arterial spin labeling MRI have been applied to image kidney hypoxia and perfusion, which might obviate the need for exogenous contrast agents.[9–13] The BOLD MRI approach maps blood oxygenation based on the increased ratio of paramagnetic deoxyhemoglobin in the capillary bed of hypoxic tissue that elicits shortening of proton T2* relaxation times.[2] However, BOLD readouts are sensitive to many factors such as the blood volume, flow rate, magnetic field inhomogeneity, or image "susceptibility" artifacts induced by hemorrhage. Moreover, the BOLD readout may not be precisely correlated with the severity of kidney dysfunction at various stages of chronic kidney disease [14]. The arterial spin labeling approaches have been proposed to elucidate kidney perfusion by quantifying the intra-renal signal derived from magnetically prepared or "labeled" segments of flowing blood.[15, 16] Although the technique might provide an accurate and reproducible readout of renal perfusion, its low signal-to-noise features are problematic for clinical application. Given these limitations, ultimately it may be the case that multi-parametric MRI with the use of BOLD, spin labeling, and/or other techniques could improve detection and quantification of intrarenal perfusion defects but at the cost of time and expense required to perform the linked studies.[11, 17, 18]

Multinuclear $^{1}H/^{19}F$ MRI coupled with perfluorocarbon (PFC) based nanoparticles (NP) represent an alternative readout applicable for imaging kidney hypoperfusion and associated injury (Figure 1).[19, 20] PFC NP are a class of clinically approved vehicles with no apparent toxic effect on the kidney.[21, 22] As a blood-pool agent, the linear relationship between the ^{19}F signal intensity and PFC NP' concentration allows *direct* measure of blood volume in tissue.[23–25] In addition, the relationship between the ^{19}F relaxation time ($R_1 = 1/T_1$) of PFC NP and dissolved O2 that alters ^{19}F relaxation linearly according to pO_2, has been utilized for in vivo assessment of pO_2 in blood and tissue[26–28]. Finally, functionalized PFC NP with the use of selected targeting ligands that can bind to and detect inflammatory markers (e.g. VCAM-1) may also allow early detection of inflammatory kidney diseases. This review offers an overview of diagnostic $^{1}H/^{19}F$ MRI with the use of PFC NP, as well as

insights into combined therapeutics with the same ^{19}F nanosystem carrying drug and gene cargoes.

B. PFC NP For Imaging

PFCs are a group of ^{19}F-containing compounds derived from hydrocarbons by partial or complete substitution of ^{1}H with ^{19}F.[29] PFCs are biologically stable, inert, well tolerated, and can carry a significant payload of O2 in dissolved form, which established their original use as blood substitutes. Liquid PFCs also have been employed as an organ preservation media for kidney transplant.[30 31, 32]

For in vivo applications, PFCs typically are emulsified into a nanoparticle form with a surfactant coating for stabilization and functionalization (Figure 1). A typical PFC NP emulsion contains 40% (v/v) PFOB, 2% (w/v) safflower oil, 2% (w/v) of surfactant commixture, 1.7% (w/v) glycerin, and water balance.[33] Thus the final formulated PFC NP comprises principally a liquid PFC core encapsulated by a lipid monolayer with a diameter of 150–250 nm and a variable surface charge depending on the types of phospholipids and surfactants used to construct it (e.g., −40 to +20 mV).

The use of PFC NP for examining tumor hypoxia has been pursued for some time and recent excellent reviews are available on the subject from pioneers in this area such as Mason.[26, 34–37] In most of these prior applications, targeting ligands have not been included as direct injections were often required to provide sufficient signal for detection of the ^{19}F signal in order to generate proof of concept for pO_2 measurements. However, as interest in the broad field of "molecular imaging" was emerging around that time, our group was the first to explore the large signal generating capacity of a nanoparticle when linked to chelated lanthanides to formulate a robust paramagnetic "bright spot" molecular MRI contrast agent.[38, 39] Because the PFC NP technology was well known and offered a ready substrate for functionalization with its surrounding lipid-surfactant surface layer, it was relatively straightforward to consider adding gadolinium complexes to the surface in large quantities (e,g., 100,000–200,000 Gd per particle), which would provide substantial signal amplification upon localization to molecular binding sites. In addition to the large cargo of Gd, a molecular targeting ligand could be added as well, where both imaging agent and targeting ligand were covalently coupled to a phospholipid anchor that was directly formulated into the particle in a single emulsification step (see specific descriptions below).

Furthermore, this PFC NP construct also was developed as the first reported ultrasound molecular imaging agent due to special features of its composition that render it visible to mechanical waves at clinically relevant imaging frequencies.[40] Fluorescence and SPECT imaging capabilities also exist for the PFC NP system when it is coupled to contrast moieties appropriate to those modalities.[41, 42]

As compared with iodinated or Gd contrast agents, PFC NP could be well suited to patients with kidney disease. PFC NP exhibit a good safety profile with minor dose dependent flu-like symptoms or fever in 24 hours after dosing. [43, 44] No renal toxicity was reported in animals and human.[22] With a nominal diameter of 250 nm, PFC NP are not susceptible to glomerular filtration but rather are removed from the circulation primarily by the

reticuloendothelial system and then the PFC component ultimately is vaporized through respiration.[21] The blood clearance half-life of PFC NP ranges from 3 to 42 hours depending the exact preparation method,[41] thereby providing sufficient time for MRI detection.

Despite the apparent utility of nanostructures carrying large payloads of Gd for T_1 weighted MRI, it was also clear that the fluorine core of the PFC NP might provide an alternative approach for magnetic resonance detection. This could represent a unique imaging signature because there is no detectable ^{19}F in the body at typical clinical field strengths. For imaging there would be no background signal as is the case for other contrast agents that rely on their effect on proton relaxation to create contrast.[45] In the case of ^{19}F imaging, quantification of the amount of PFC NP in the imaging field of view is possible by directly assessing the spectral energy contained within the ^{19}F readout, which is proportional to the ^{19}F concentration, and thus the number of PFC NP containing them.[46–49] Thus, the non-targeted PFC NP agents have been developed for blood pool imaging and perfusion,[46–48, 50] cellular (stem cell, dendritic cell, etc.) labeling and tracking,[49, 51–55] cellular and tissue uptake for imaging inflammation and allograft rejection, among others. [56, 57]

Elucidation of Kidney Function and Injury with PFC NP

Hypoxic/ischemic injury is a common pathology in acute and chronic kidney diseases.[35, 58–60] Some contributing factors include: interstitial fibrosis that increases the diffusion distance of O2 from capillaries to tubular epithelial cells,[61] vessel rarefraction that reduces the capillary density,[62] arterial stenosis that can reduce the overall amount of blood delivered to the kidney,[63] and acute thrombosis that blocks regional blood flow. Hypoxic/ischemic injury may develop regionally, e.g. in the cortex or medulla,[61] but nevertheless still affect the global renal function. This regional manifestation of the disease process can pose a challenge to the precise elucidation of the disease process and stage when only global kidney functional readouts are available such as GFR or blood/urine markers.[64] We therefore have proposed that non-invasive regional mapping of kidney oxygenation could be beneficial for understanding the disease process and for clinical management that may be stage and molecular pathway specific.

Quantitative ^{19}F MRI using PFCs or PFC NP has been extensively exploited for *in vivo* imaging of hypoxia.[29, 35] PFCs can carry a high payload of O_2 that exhibit a linear dissociation curve, which renders them potential reporters for local pO_2 such that at a given temperature, the partial pressure of dissolved paramagnetic O_2 in PFCs is linearly correlated with the ^{19}F relaxation rate.[65] The exchange of O_2 between PFCs and surrounding media occurs through free diffusion operating on a millisecond timescale.[66] It is straightforward to generate a calibration curve specifying the relationship between ^{19}F R_1 and pO_2 at a given field strength in order to read out the pO_2 to provide a non-invasive measure of tissue oxygenation.[67] In solid tumor where tissue temperature is heterogeneous, hexafluorobenzene and perfluoropolyether that exhibit minimal sensitivity of ^{19}F R1 to temperature changes between 30 and 42°C are typically used for ^{19}F MRI oximetry.[68] The precision of ^{19}F MRI oximetry may be within 1–3 mmHg and the absolute readout of pO_2 is comparable to that measured with fiberoptic,[69] and near-infrared spectroscopy[70, 71] in tumor tissues.

Recently, fast ^{19}F MRI techniques like FREDOM (Fluorocarbon Relaxometry using Echo planar imaging for Dynamic Oxygen Mapping) and BESR (Blood Enhanced Saturation Recovery) have been developed to facilitate in vivo mapping of pO_2,[72–74] which should be applicable for kidney imaging and pO_2 measurements. Our approach using the BESR method mirrors some existing methods for defining proton relaxivity in vivo but takes advantage of flowing blood to quantize the ^{19}F signal that is moving rather than stationary, which facilitates correlation of the detected signal with blood volume, blood flow, and regional pO_2.[74] Figure 2 shows the effect on the MRI signal intensity for ^{19}F in circulating PFC NP as it is affected by blood pO_2. The presaturated (darker cardiac chambers at left side of panels) ^{19}F spins in the heart recover (i.e., brighten) more quickly as the signal is measured over 2 seconds under conditions of hyperoxia (lower panels) than of normoxia (upper panels). Moreover, the signal in the RV recovers more slowly than that in the LV due to the inherently lower pO_2 in the RV chamber under all conditions. The quantification of LV and RV pO_2 matches well with the expected values under each condition. These types of measurements in the kidney should now be possible in vivo in actual patients due to the recent implementation of similar approaches on clinical 3T MRI scanners that can acquire simultaneous ^{1}H and ^{19}F signals for mapping PFC NP concentrations, regional pO_2,[75] arterio-venous differences in pO_2[74] or blood volume fraction,[76], therefore to derive global renal oxygen consumption.

Moving on to the kidney itself, we have employed an acute kidney injury model and applied ^{19}F MRI in conjunction with PFC NP to assess ischemic injury and the consequences of regional hypoperfusion.[77] The objective here is to develop a multi-nuclear $^{1}H/^{19}F$ MRI approach for functional renal imaging. We first demonstrated the feasibility of ^{19}F MR mapping of renal blood volume and pO_2 in healthy mouse kidneys (Figure 3. Left panel). Subsequently, a unilateral renal ischemia-reperfusion model of AKI[78] to demonstrate that transient ischemia damages endothelial and tubular cells causing sustained medullary microvessel non-perfusion[79] and tubular ischemia.[80–82] The result of this study showed that ^{19}F MRI sensitively detected decreased renal blood volume in the cortical-medullary (CM) junction, where ^{1}H BOLD MRI also detected increased T2* reflecting reduced susceptibility effect from blood flow. (Figure 3. Right panel). The follow-up histology analysis confirmed a reduced density of perfused blood vessels in the CM junction of injured kidneys. The intrarenal blood pO_2, however, remained unchanged, which may attributed to the capability of kidney to auto-regulate perfusion to maintain oxygenation despite the reduction of blood flow.[1, 83]

Our previous work have demonstrated the feasibility of in vivo ^{19}F MRI angiography in rabbits on a 1.5T Philips clinical MR system.[50] Given the high blood volume in the kidney and the availability of 3T clinical MR consoles, ^{19}F MRI assessment of kidney blood volume and pO_2 should be achievable in clinical settings.

Potential Molecular Imaging Applications For Targeted PFC NP

The panoply of molecular imaging applications for kidney disease that can be addressed with the use of targeted contrast agents is extensive. Here we review some indications for

targeted PFC NP that are directly related to or associated with important comorbid conditions that apply to progressive renal disease.

Atherosclerosis—The role of atherosclerosis in predisposing to acute and chronic renal failure under many conditions is clear.[60, 84] Moreover, the inflammatory milieu in both early and advanced plaques can be addressed with ^{19}F imaging in several ways. We have shown recently that non-targeted PFC NP can diffuse passively into the core of intimal plaques where vascular barrier disruption has occurred over time as a consequence of endothelial damage, apoptosis, and cellular sloughing.[56] Indeed, in the later stages of the disease process in fat fed rabbits for example, massive infiltration of nanoparticles into the plaque extending up to the medial boundary can occur in vivo, and be detected with ^{19}F MRI, indicating the ready access of blood coagulation elements to a hypercoagulable inflamed plaque milieu, predisposing to acute and/or chronic thrombosis (Figure 4). Similar passive penetration into human carotid endarterectomy samples excised for clinical indications in symptomatic patients mimicked the experimental detection of endothelial barrier disruption. These data suggest that vascular endothelial disruption in acute kidney injury might similarly be amenable to quantification with ^{19}F MRI, as we showed above for nanoparticles passively penetrating the renal interstitium in ischemic injury.

Alternatively, angiogenesis imaging is possible with a number of modalities including MRI, PET, SPECT, and ultrasound.[85–87] The role of plaque neovasculature that is driven by tissue/macrophage hypoxia is known to be required for early plaque growth and predisposes to late plaque rupture and subsequent thrombosis and acute vessel occlusion.[88–92] For example, in experimental atherosclerosis in fat fed rabbits, the neovasculature emerging from the inflamed adventitial vasa vasorum can be detected and quantified by MRI with Gd-conjugated NP targeted to upregulated endothelial integrins (Figure 5) at clinical field strengths.[39, 93–95] The same agents have been used for tumor angiogenesis imaging, which also have been detected in vivo with ^{19}F MRI.[96]

Neovasculature expressing heterodimeric molecular epitopes such as $\alpha_v\beta_3$ integrins also has been detected sensitively with ultrasound imaging in experimental models.[97–99] In a genetic model of squamous cell carcinoma, extremely limited extents of inflammatory neovasculature could be demonstrated in the mouse pinna with high resolution ultrasound imaging systems and special signal processing algorithms that harbor quantitative potential based on the "information content" of the data stream.[98–100] Both pathological (e.g., atherosclerosis, cancer, inflammation) and tissue reparative processes (e.g., recovery from ischemic injury) invoke significant angiogenesis that might be candidates for renal imaging,

An array of other inflammatory molecules involved in atherosclerosis might be amenable to noninvasive molecular imaging. For example, we have used ^{19}F MRI to detect the upregulation of renal vascular VCAM-1 in mice fed a Western diet for 35 weeks (Figure 6).[101] Because VCAM and other related adhesion molecules are responsible for trafficking of immune effector cells such as monocytes and neutrophils to areas of damage and inflammation, assessment of the potential for cellular recruitment in kidney injury might be useful disease staging and optimization of therapeutic approaches. Ultrasound approaches with targeted microbubbles containing a *gaseous* perfluorocarbon also have been

demonstrated for renal VCAM imaging,[102] although there is lesser potential for quantification.

Thrombosis—Fibrin detection in formed clots also has been demonstrated in vivo with ultrasound at clinical frequencies after binding of PFC NP targeted to selected fibrin epitopes, again with a monoclonal antibody.[38, 40, 103] Because fibrin clots are barely echogenic and therefore difficult to detect with clinical ultrasound, this could be useful for renal diseases that are prone to thrombosis such as hemolytic uremic syndrome, AKI, sepsis, atherosclerosis, etc. Additional examples of fibrin imaging have been reported with the use of MRI by detection of either the 1H or ^{19}F signatures of PFC NP (Figure 7) [47, 104–106] As compared with standard ultrasound molecular imaging, the MRI readouts for ^{19}F are quantitative and can be expressed in molar concentrations of bound nanoparticles or fluorine atoms (see Figure 7) permitting longitudinal determination of the local concentration of targeted molecular epitopes.

The presence of thrombin itself in newly forming clots can be delineated with thrombin targeted PFC NP imaged with MRI.[107] Thrombin is the key regulator of clot formation because it converts fibrinogen to fibrin locally after being activated on an acute clotting surface by factor Xa. Nanoparticles bearing a small, modified peptide, PPACK (phenylalanine-proline-arginine-chloromethylketone), can covalently couple to the active pocket of thrombin molecules within forming clots and can be imaged dynamically and quantified with ^{19}F MRI (Figure 8). Another advantage of this approach concerns the role of thrombin as a signaling molecule operating through protease activated receptors (e.g., PAR-1) that participate in signaling events in inflammation, atherosclerosis, and thrombosis, potentially conferring the capability to noninvasively delineate certain molecular regulatory pathways that might attend selected renal pathologies.

Ultrasound molecular imaging with targeted liquid PFC NP has been reported to detect other constituents of thromboembolic disease. For example, Tissue Factor (TF), which is the proximate cause of thrombosis during plaque rupture and is also associated with microangiopathic renal thrombosis in AKI and other kidney diseases, is detectable in vascular segments exposed to balloon injury that incites inflammation and upregulation of TF in the media layer (Figure 9).[108–111] In this case, the selective binding and deposition of PFC NP are targeted to TF with the use of a specific conjugated monoclonal antibody fragment.

Cellular imaging with PFC NP labeled immune, stem, and vascular precursor cells represents another opportunity for addressing inflammatory pathologies or regenerative approaches for therapy. A variety of cell types are capable of being isolated, subjected to PFC NP labeling by endocytosis in vivo, and then reinjected either locally into tissues or systemically where they can be tracked by ^{19}F MRI.[49, 51, 52, 55, 112–114] Figure 10 shows an example of two distinct PFC labels in endothelial precursor cells that contribute to tumor angiogenesis, and illustrates the opportunity for tracking multiple cell labels simultaneously. In other example, Ahrens and collaborators have mapped acute allograft rejection with ^{19}F labeled immune cells.[57] Such strategies might exhibit clear significance for kidney transplantation or for defining immunologically driven kidney pathologies.

A limitation for molecular ^{19}F MRI is the low signal from targeted/localized PFC NP. To reduce imaging time in clinical settings, Gd-DTPA conjugated PFC NP maybe used for fast molecular ^{1}H MRI to detect targeted/localized PFC NP, while a low resolution ^{19}F MRI or MRS can be used to quantify the amount of PFC NP. Since Gd-DTPA is associated with increased frequency of acute adverse reactions, the safety profile and optimal dosage of Gd-DTPA loaded PFC NP in patients with kidney injury needs to be evaluated.

Therapeutics with PFC NP

A brief mention of the therapeutic utility of PFC NP is warranted, as both imaging and therapy can be combined to good effect with this system due to the ability to quantify drug deposition based on ^{19}F spectroscopy. In other words, by knowing how much drug or gene product is present per nanoparticle and measuring the concentration of NP by ^{19}F MRI as per reported methodologies,[47, 48, 115] one can estimate the dose of drug deposited at any given time in an imaging voxel. A selected listing of some of the agents that have been used in various diseases in conjunction with therapeutic PFC NP is shown in Table 1. Moreover, it is worth noting that most of the formulations have been molecularly targeted to enhance local deposition and retention in the selected tissues with the use of preselected targeting ligands that are prepared in a one step process along with the therapeutic agent. However, we have demonstrated that it is feasible to prepare a base imaging and/or therapeutic agent and choose the targeting ligand later for "postformulation targeting" with a membrane inserting peptide cargo carrier,[116–118] which allows great flexibility in selection of targets based on changing conditions as diseases progress through different stages. This feature is expected to facilitate more personalized approaches to nanomedicine in the future.

Limitations and Challenges

For imaging renal perfusion, ^{19}F MRI requires longer imaging time (minutes to tens of minutes) than ^{1}H MRI techniques like ASL and DCE enhanced MRI (takes seconds to a few minutes). The use of PFC NP as a contrast agent will also incur extra cost. However, the unique advantage of ^{19}F MRI is its capability to directly mapping intrarenal blood volume since the 19F signal intensity is linearly correlated with the quantity of PFC NP in each voxel. When a ^{19}F inversion-recovery gradient echo sequence was employed to measuring pO_2, the ^{19}F signal from PFC NP are contributed by both artery and veins. [74] Alternatively, the signal from fast moving PFC NP in arterial blood flow can be suppressed by employing spin echo acquisitions. [77] The detected ^{19}F signal are primary contributed by PFC NP in capillaries and veins. Similar to the limitation of BOLD MRI, the limitation of ^{19}F MRI is that it detects blood pO_2. It is yet unknown how accurately blood pO_2 reflects tissue pO_2.[119] Finally, translating PFC NP to clinical settings is limited by the low sensitivity of ^{19}F signal on the “low field” (e.g. 3T) clinical MR scanner, which may require prolonged imaging time (tens of minutes) to achieve satisfactory signal to noise ratio. This will pose practical problems to image AKI patients who are in critical condition and require intensive care. The motion artifact from bowel movement and respiration during image acquisition should be also corrected for image reconstruction. [96]

Acknowledgments

We acknowledge the financial support from NIH grants R01 HL073646 and R21 DK095555 to Wickline SA.

References

1. Gloviczki ML, Glockner JF, Lerman LO, et al. Preserved oxygenation despite reduced blood flow in poststenotic kidneys in human atherosclerotic renal artery stenosis. Hypertension. 2010; 55(4):961–966. [PubMed: 20194303]
2. Prasad PV. Functional MRI of the kidney: tools for translational studies of pathophysiology of renal disease. Am J Physiol Renal Physiol. 2006; 290(5):F958–F974. [PubMed: 16601297]
3. Kalantarinia K. Novel imaging techniques in acute kidney injury. Curr Drug Targets. 2009; 10(12): 1184–1189. [PubMed: 19715540]
4. Tsushima Y. Functional CT of the kidney. Eur J Radiol. 1999; 30(3):191–197. [PubMed: 10452717]
5. Briguori C, Marenzi G. Contrast-induced nephropathy: pharmacological prophylaxis. Kidney Int Suppl. 2006; (100):S30–s38. [PubMed: 16612399]
6. Briguori C, Visconti G, Focaccio A, et al. Renal Insufficiency After Contrast Media Administration Trial II (REMEDIAL II): RenalGuard System in high-risk patients for contrast-induced acute kidney injury. Circulation. 2011; 124(11):1260–1269. [PubMed: 21844075]
7. Gleeson TG, Bulugahapitiya S. Contrast-induced nephropathy. AJR Am J Roentgenol. 2004; 183(6):1673–1689. [PubMed: 15547209]
8. Wong PC, Li Z, Guo J, Zhang A. Pathophysiology of contrast-induced nephropathy. Int J Cardiol. 2012; 158(2):186–192. [PubMed: 21784541]
9. Grenier N, Basseau F, Ries M, et al. Functional MRI of the kidney. Abdom Imaging. 2003; 28(2): 164–175. [PubMed: 12592462]
10. Maril N, Rosen Y, Reynolds GH, et al. Sodium MRI of the human kidney at 3 tesla. Magn Reson Med. 2006; 56(6):1229–1234. [PubMed: 17089361]
11. Ries M, Basseau F, Tyndal B, et al. Renal diffusion and BOLD MRI in experimental diabetic nephropathy. Blood oxygen level-dependent. J Magn Reson Imaging. 2003; 17(1):104–113. [PubMed: 12500279]
12. Rossi C, Sharma P, Pazahr S, et al. Blood Oxygen Level-Dependent Magnetic Resonance Imaging of the Kidneys: Influence of Spatial Resolution on the Apparent R2* Transverse Relaxation Rate of Renal Tissue. Invest Radiol. 2013
13. Ritt M, Janka R, Schneider MP, et al. Measurement of kidney perfusion by magnetic resonance imaging: comparison of MRI with arterial spin labeling to para-aminohippuric acid plasma clearance in male subjects with metabolic syndrome. Nephrol Dial Transplant. 2010; 25(4):1126–1133. [PubMed: 19934080]
14. Pruijm M, Hofmann L, Vogt B, et al. Renal tissue oxygenation in essential hypertension and chronic kidney disease. Int J Hypertens. 2013; 2013:696598. [PubMed: 23509612]
15. Detre JA, Zhang WG, Roberts DA, et al. Tissue specific perfusion imaging using arterial spin labeling. NMR in Biomedicine. 1994; 7(1–2):75–82. [PubMed: 8068529]
16. Liu YP, Song R, Liang C, Chen X, Liu B. Arterial spin labeling blood flow magnetic resonance imaging for evaluation of renal injury. Am J Physiol Renal Physiol. 2012; 303(4):F551–F558. [PubMed: 22647631]
17. Wu WC, Su MY, Chang CC, Tseng WY, Liu KL. Renal perfusion 3-T MR imaging: a comparative study of arterial spin labeling and dynamic contrast-enhanced techniques. Radiology. 2011; 261(3):845–853. [PubMed: 22095996]
18. Chandarana H, Lee VS. Renal Functional MRI: Are We Ready for Clinical Application? American Journal of Roentgenology. 2009; 192(6):1550–1557. [PubMed: 19457818]
19. Chen J, Lanza GM, Wickline SA. Quantitative magnetic resonance fluorine imaging: today and tomorrow. Wiley Interdiscip Rev Nanomed Nanobiotechnol. 2010; 2(4):431–440. [PubMed: 20564465]

20. Wickline, SA.; Mason, RP.; Caruthers, SD., et al. Fluorocarbon agents for multimodal molecular imaging and targeted therapeutics. In: Weissleder, R., et al., editors. MOLECULAR IMAGING: PRINCIPLES AND PRACTICE. Shelton, CT: Peoples Medical Publishing House-USA; 2010. p. 542-573.
21. Cohn CS, Cushing MM. Oxygen therapeutics: perfluorocarbons and blood substitute safety. Crit Care Clin. 2009; 25(2):399–414. Table of Contents. [PubMed: 19341916]
22. Spahn DR. Blood substitutes. Artificial oxygen carriers: perfluorocarbon emulsions. Crit Care. 1999; 3(5):R93–R97. [PubMed: 11094488]
23. Baldwin NJ, Wang Y, Ng TC. In situ 19F MRS measurement of RIF-1 tumor blood volume: corroboration by radioisotope-labeled [125I]-albumin and correlation to tumor size. Magn Reson Imaging. 1996; 14(3):275–280. [PubMed: 8725193]
24. Gu Y, Mason R, Liu H. Estimated fraction of tumor vascular blood contents sampled by near infrared spectroscopy and 19F magnetic resonance spectroscopy. Opt Express. 2005; 13(5):1724–1733. [PubMed: 19495051]
25. Thomas C, Counsell C, Wood P, Adams GE. Use of fluorine-19 nuclear magnetic resonance spectroscopy and hydralazine for measuring dynamic changes in blood perfusion volume in tumors in mice. J Natl Cancer Inst. 1992; 84(3):174–180. [PubMed: 1542128]
26. Mason RP. Noninvasive physiology: ^{19}F NMR of perfluorocarbon. Art. Cells, Blood Sub. & Immob. Biotech. 1994; 22(4):1141–1153.
27. Mason RP, Antich PP, Babcock EE, et al. Noninvasive determination of tumor oxygen tension and local variation with growth. Int J Radiat Oncol Biol Phys. 1994; 29(1):95–103. [PubMed: 8175452]
28. Zhao D, Jiang L, Mason RP. Measuring changes in tumor oxygenation. Methods Enzymol. 2004; 386:378–418. [PubMed: 15120262]
29. Spiess BD. Perfluorocarbon emulsions as a promising technology: a review of tissue and vascular gas dynamics. J Appl Physiol. 2009; 106(4):1444–1452. [PubMed: 19179651]
30. Kaneda MM, Caruthers S, Lanza GM, Wickline SA. Perfluorocarbon nanoemulsions for quantitative molecular imaging and targeted therapeutics. Ann Biomed Eng. 2009; 37(10):1922–1933. [PubMed: 19184435]
31. Hosgood SA, Nicholson ML. The role of perfluorocarbon in organ preservation. Transplantation. 2010; 89(10):1169–1175. [PubMed: 20393403]
32. Marada T, Zacharovova K, Saudek F. Perfluorocarbon improves post-transplant survival and early kidney function following prolonged cold ischemia. Eur Surg Res. 2010; 44(3–4):170–178. [PubMed: 20339301]
33. Morawski AM, Winter P, Yu X, et al. Quantitative Magnetic Resonance Immunohistochemistry with Ligand-Targeted 19F Nanoparticles. Magn Reson Med. 2004; 52:1255–1262. [PubMed: 15562481]
34. Mason RP, Antich PP, Babcock EE, Gerberich JL, Nunnally RL. Perfluorocarbon imaging in vivo: An ^{19}F MRI study in tumor-bearing mice. Mag Res Imaging. 1989; 7:475–485.
35. Mason RP, Ran S, Thorpe PE. Quantitative assessment of tumor oxygen dynamics: Molecular Imaging for Prognostic Radiology. J. Cell. Biochem. 2002; 87(suppl):45–53.
36. Ruiz-Cabello J, Barnett BP, Bottomley PA, Bulte JW. Fluorine (19F) MRS and MRI in biomedicine. NMR Biomed. 2011; 24(2):114–129. [PubMed: 20842758]
37. Yu JX, Hallac RR, Chiguru S, Mason RP. New frontiers and developing applications in 19F NMR. Prog Nucl Magn Reson Spectrosc. 2013; 70:25–49. [PubMed: 23540575]
38. Lanza GM, Lorenz CH, Fischer SE, et al. Enhanced detection of thrombi with a novel fibrin-targeted magnetic resonance imaging agent. Academic Radiology. 1998; 5:S173–S176. [PubMed: 9561074]
39. Winter P, Athey P, Kiefer G, et al. Improved paramagnetic chelate for molecular imaging with MRI. Journal of Magnetism and Magnetic Materials. 2005; 293(1):540–545.
40. Lanza GM, Wallace KD, Scott MJ, et al. A novel site-targeted ultrasonic contrast agent with broad biomedical application. Circulation. 1996; 94(12):3334–3340. [PubMed: 8989148]

41. Hu G, Lijowski M, Zhang H, Partlow KC, Caruthers SD, Kiefer G, Gulyas G, Athey P, Scott MJ, Wickline SA, Lanza GM. Imaging of Vx-2 rabbit tumors with αvβ3-integrin-targeted 111In nanoparticles. International Journal of Cancer. 2007; 120:1951–1957.
42. Lijowski M, Caruthers S, Hu G, et al. High sensitivity: High-resolution SPECT-CT/MR molecular imaging of angiogenesis in the Vx2 model. Investigative Radiology. 2009; 44(1):15–22. [PubMed: 18836386]
43. Keipert PE, Otto S, Flaim SF, et al. Influence of perflubron emulsion particle size on blood half-life and febrile response in rats. Artif Cells Blood Substit Immobil Biotechnol. 1994; 22(4):1169–1174. [PubMed: 7849919]
44. Noveck RJ, Shannon EJ, Leese PT, et al. Randomized safety studies of intravenous perflubron emulsion. II. Effects on immune function in healthy volunteers. Anesth Analg. 2000; 91(4):812–822. [PubMed: 11004031]
45. Chen J, Wickline SA, Lanza GM. Quantitative Magnetic Resonance Fluorine Imaging: Today and tomorrow. WIRE Nanomed Nanobiotechnol. 2010
46. Morawski AM, Lanza GA, Wickline SA. Targeted contrast agents for magnetic resonance imaging and ultrasound. Curr Opin Biotechnol. 2005; 16(1):89–92. [PubMed: 15722020]
47. Morawski AM, Winter PM, Yu X, et al. Quantitative “magnetic resonance immunohistochemistry” with ligand-targeted ^{19}F nanoparticles. Magn Reson Med. 2004; 52:1255–1262. [PubMed: 15562481]
48. Morawski AM, Winter PM, Crowder KC, et al. Targeted nanoparticles for quantitative imaging of sparse molecular epitopes with MRI. Magn Reson Med. 2004; 51:480–486. [PubMed: 15004788]
49. Partlow KC, Chen J, Brant JA, et al. 19F magnetic resonance imaging for stem/progenitor cell tracking with multiple unique perfluorocarbon nanobeacons. FASEB J. 2007; 21(8):1647–1654. Epub 2007 Feb 6. [PubMed: 17284484]
50. Neubauer AM, Caruthers SD, Hockett FD, et al. Fluorine cardiovascular magnetic resonance angiography in vivo at 1.5 T with perfluorocarbon nanoparticle contrast agents. J Cardiovasc Magn Reson. 2007; 9(3):565–573. [PubMed: 17365236]
51. Ahrens ET, Flores R, Xu H, Morel PA. In vivo imaging platform for tracking immunotherapeutic cells. Nat Biotechnol. 2005; 23(8):983–987. [PubMed: 16041364]
52. Ruiz-Cabello J, Walczak P, Kedziorek DA, et al. In vivo "hot spot" MR imaging of neural stem cells using fluorinated nanoparticles. Magn Reson Med. 2008; 60(6):1506–1511. [PubMed: 19025893]
53. Bonetto F, Srinivas M, Heerschap A, et al. A novel (19)F agent for detection and quantification of human dendritic cells using magnetic resonance imaging. Int J Cancer. 2011; 129(2):365–373. [PubMed: 20839261]
54. Helfer BM, Balducci A, Nelson AD, et al. Functional assessment of human dendritic cells labeled for in vivo (19)F magnetic resonance imaging cell tracking. Cytotherapy. 2010; 12(2):238–250. [PubMed: 20053146]
55. Janjic JM, Ahrens ET. Fluorine-containing nanoemulsions for MRI cell tracking. Wiley Interdiscip Rev Nanomed Nanobiotechnol. 2009; 1(5):492–501. [PubMed: 19920872]
56. Zhang H, Zhang L, Myerson J, et al. Quantifying the evolution of vascular barrier disruption in advanced atherosclerosis with semipermeant nanoparticle contrast agents. PLoS One. 2011; 6(10):e26385. [PubMed: 22028868]
57. Hitchens TK, Ye Q, Eytan DF, et al. 19F MRI detection of acute allograft rejection with in vivo perfluorocarbon labeling of immune cells. Magn Reson Med. 2011; 65(4):1144–1153. [PubMed: 21305593]
58. Krohn KA, Link JM, Mason RP. Molecular imaging of hypoxia. J Nucl Med. 2008; 49(Suppl 2): 29S–48S.
59. Garovic VD, Textor SC. Renovascular hypertension and ischemic nephropathy. Circulation. 2005; 112(9):1362–1374. [PubMed: 16129817]
60. Lerman LO, Textor SC, Grande JP. Mechanisms of tissue injury in renal artery stenosis: ischemia and beyond. Prog Cardiovasc Dis. 2009; 52(3):196–203. [PubMed: 19917330]
61. Palm F, Nordquist L. Renal tubulointerstitial hypoxia: cause and consequence of kidney dysfunction. Clin Exp Pharmacol Physiol. 2011; 38(7):474–480. [PubMed: 21545630]

62. Lindenmeyer MT, Kretzler M, Boucherot A, et al. Interstitial vascular rarefaction and reduced VEGF-A expression in human diabetic nephropathy. J Am Soc Nephrol. 2007; 18(6):1765–1776. [PubMed: 17475821]
63. Gloviczki ML, Glockner JF, Crane JA, et al. Blood oxygen level-dependent magnetic resonance imaging identifies cortical hypoxia in severe renovascular disease. Hypertension. 2011; 58(6): 1066–1072. [PubMed: 22042812]
64. Inoue T, Kozawa E, Okada H, et al. Noninvasive evaluation of kidney hypoxia and fibrosis using magnetic resonance imaging. J Am Soc Nephrol. 2011; 22(8):1429–1434. [PubMed: 21757771]
65. Mason RP, Shukla H, Antich PP. In vivo oxygen tension and temperature: simultaneous determination using 19F NMR spectroscopy of perfluorocarbon. Magn Reson Med. 1993; 29(3): 296–302. [PubMed: 8450738]
66. O'Brien RN, Langlais AJ, Seufert WD. Diffusion coefficients of respiratory gases in a perfluorocarbon liquid. Science. 1982; 217(4555):153–155. [PubMed: 6806902]
67. Zhang W, Ito Y, Berlin E, Roberts R, Berkowitz BA. Role of hypoxia during normal retinal vessel development and in experimental retinopathy of prematurity. Invest Ophthalmol Vis Sci. 2003; 44(7):3119–3123. [PubMed: 12824260]
68. Kodibagkar VD, Wang X, Mason RP. Physical principles of quantitative nuclear magnetic resonance oximetry. Front Biosci. 2008; 13:1371–1384. [PubMed: 17981636]
69. Zhao D, Constantinescu A, Hahn EW, Mason RP. Tumor oxygen dynamics with respect to growth and respiratory challenge: investigation of the Dunning prostate R3327-HI tumor. Radiat Res. 2001; 156(5 Pt 1):510–520. [PubMed: 11604064]
70. Kim JG, Zhao D, Song Y, et al. Interplay of tumor vascular oxygenation and tumor pO2 observed using near-infrared spectroscopy, an oxygen needle electrode, and 19F MR pO2 mapping. J Biomed Opt. 2003; 8(1):53–62. [PubMed: 12542380]
71. Xia M, Kodibagkar V, Liu H, Mason RP. Tumour oxygen dynamics measured simultaneously by near-infrared spectroscopy and 19F magnetic resonance imaging in rats. Phys Med Biol. 2006; 51(1):45–60. [PubMed: 16357430]
72. Hunjan S, Zhao D, Constantinescu A, et al. Tumor oximetry: demonstration of an enhanced dynamic mapping procedure using fluorine-19 echo planar magnetic resonance imaging in the Dunning prostate R3327-AT1 rat tumor. Int J Radiat Oncol Biol Phys. 2001; 49(4):1097–1108. [PubMed: 11240252]
73. Jordan BF, Cron GO, Gallez B. Rapid monitoring of oxygenation by 19F magnetic resonance imaging: Simultaneous comparison with fluorescence quenching. Magn Reson Med. 2009; 61(3): 634–638. [PubMed: 19097235]
74. Hu L, Chen J, Yang X, et al. Rapid quantification of oxygen tension in blood flow with a fluorine nanoparticle reporter and a novel blood flow-enhanced-saturation-recovery sequence. Magn Reson Med. 2012
75. Shukla HP, Mason RP, Bansal N, Antich PP. Regional myocardial oxygen tension: 19F MRI of sequestered perfluorocarbon. Magn Reson Med. 1996; 35(6):827–833. [PubMed: 8744009]
76. Duong TQ, Kim SG. In vivo MR measurements of regional arterial and venous blood volume fractions in intact rat brain. Magn Reson Med. 2000; 43(3):393–402. [PubMed: 10725882]
77. Hu L, Chen J, Yang X, et al. Assessing Intrarenal Non-perfusion and Vascular Leakage in Acute Kidney Injury with multi-nuclear 1H/19F MRI and Perfluorocarbon Nanoparticles. Magn Reson Med. 2013; 2013
78. Paller MS, Murray BM. Renal dysfunction in animal models of cyclosporine toxicity. Transplant Proc. 1985; 17(4 Suppl 1):155–159. [PubMed: 3895656]
79. Mason J, Torhorst J, Welsch J. Role of the medullary perfusion defect in the pathogenesis of ischemic renal failure. Kidney Int. 1984; 26(3):283–293. [PubMed: 6513274]
80. Devarajan P. Update on mechanisms of ischemic acute kidney injury. J Am Soc Nephrol. 2006; 17(6):1503–1520. [PubMed: 16707563]
81. Basile DP. The endothelial cell in ischemic acute kidney injury: implications for acute and chronic function. Kidney Int. 2007; 72(2):151–156. [PubMed: 17495858]

82. Basile DP, Donohoe D, Roethe K, Osborn JL. Renal ischemic injury results in permanent damage to peritubular capillaries and influences long-term function. Am J Physiol Renal Physiol. 2001; 281(5):F887–F899. [PubMed: 11592947]
83. Leong CL, Anderson WP, O'Connor PM, Evans RG. Evidence that renal arterial-venous oxygen shunting contributes to dynamic regulation of renal oxygenation. Am J Physiol Renal Physiol. 2007; 292(6):F1726–F1733. [PubMed: 17327497]
84. Stinghen AE, Pecoits-Filho R. Vascular damage in kidney disease: beyond hypertension. Int J Hypertens. 2011; 2011:232683. [PubMed: 21876786]
85. Lanza GM, Winter PM, Caruthers SD, et al. Nanomedicine opportunities for cardiovascular disease with perfluorocarbon nanoparticles. Nanomedicine (London, England). 2006; 1(3):321–329.
86. Lanza GM, Winter PM, Caruthers SD, et al. Theragnostics for tumor and plaque angiogenesis with perfluorocarbon nanoemulsions. Angiogenesis. 2010; 13(2):189–202. [PubMed: 20411320]
87. Lanza GM, Winter PM, Hughes MS, et al. Molecular imaging and therapy: New paradigms for 21st century medicine. Polymeric Drug Delivery I: Particulate Drug Carriers. 2006
88. Moulton KS, Vakili K, Zurakowski D, et al. Inhibition of plaque neovascularization reduces macrophage accumulation and progression of advanced atherosclerosis. Proc Natl Acad Sci U S A. 2003; 100(8):4736–4741. [PubMed: 12682294]
89. Moreno PR, Purushothaman KR, Sirol M, Levy AP, Fuster V. Neovascularization in human atherosclerosis. Circulation. 2006; 113(18):2245–2252. [PubMed: 16684874]
90. Jain RK, Finn AV, Kolodgie FD, Gold HK, Virmani R. Antiangiogenic therapy for normalization of atherosclerotic plaque vasculature: a potential strategy for plaque stabilization. Nat Clin Pract Cardiovasc Med. 2007; 4(9):491–502. [PubMed: 17712362]
91. Kolodgie FD, Gold HK, Burke AP, et al. Intraplaque Hemorrhage and Progression of Coronary Atheroma. New England Journal of Medicine. 2003; 349(24):2316–2325. [PubMed: 14668457]
92. Virmani R, Kolodgie FD, Burke AP, et al. Atherosclerotic plaque progression and vulnerability to rupture: Angiogenesis as a source of intraplaque hemorrhage. Arteriosclerosis, Thrombosis, and Vascular Biology. 2005; 25(10):2054–2061.
93. Winter PM, Cai K, Caruthers SD, Wickline SA, Lanza GM. Emerging nanomedicine opportunities with perfluorocarbon nanoparticles. Expert Review of Medical Devices. 2007; 4(2):137–145. [PubMed: 17359221]
94. Winter PM, Caruthers SD, Kassner A, et al. Molecular imaging of angiogenesis in nascent Vx-2 rabbit tumors using a novel alpha(nu)beta3-targeted nanoparticle and 1.5 tesla magnetic resonance imaging. Cancer Res. 2003; 63(18):5838–5843. [PubMed: 14522907]
95. Winter PM, Schmieder AH, Caruthers SD, et al. Minute dosages of αvβ3-targeted fumagillin nanoparticles impair Vx-2 tumor angiogenesis and development in rabbits. FASEB J. 2008; 22:2758–2767. [PubMed: 18362202]
96. Keupp J, Rahmer J, Grasslin I, et al. Simultaneous dual-nuclei imaging for motion corrected detection and quantification of 19F imaging agents. Magn Reson Med. 2011; 66(4):1116–1122. [PubMed: 21394779]
97. Hughes M, Caruthers S, Tran T, et al. Perfluorocarbon nanoparticles for molecular imaging and targeted therapeutics. Proceedings of the IEEE. 2008; 96(3):397–415.
98. Hughes MS, Marsh JN, Arbeit JM, et al. Application of Renyi entropy for ultrasonic molecular imaging. J Acoust Soc Am. 2009; 125(5):3141–3145. [PubMed: 19425656]
99. Hughes MS, McCarthy JE, Marsh JN, et al. Properties of an entropy-based signal receiver with an application to ultrasonic molecular imaging. Journal of the Acoustical Society of America. 2007; 121(6):3542–3557. [PubMed: 17552706]
100. Hughes MS, McCarthy JE, Wickerhauser MV, et al. Real-time calculation of a limiting form of the Renyi entropy applied to detection of subtle changes in scattering architecture. Journal of the Acoustical Society of America. 2009; 126(5):2350–2358. [PubMed: 19894818]
101. Southworth R, Kaneda M, Chen J, et al. Renal vascular inflammation induced by western diet in ApoE-null mice quantified by 19F NMR of VCAM-1 targeted nanobeacons. Nanomedicine: Nanotechnology, Biology, and Medicine. 2009; 5(3):359–367.

102. Lindner JR. Molecular imaging with contrast ultrasound and targeted microbubbles. J Nucl Cardiol. 2004; 11(2):215–221. [PubMed: 15052252]
103. Lanza GM, Wickline SA. Targeted ultrasonic contrast agents for molecular imaging and therapy. Progress In Cardiovascular Disease. 2001; 44:13–31. [PubMed: 11533924]
104. Caruthers SD, Neubauer AM, Hockett FD, et al. In Vitro Demonstration Using 19F Magnetic Resonance to Augment Molecular Imaging With Paramagnetic Perfluorocarbon Nanoparticles at 1.5 Tesla. Invest Radiol. 2006; 41:305–312. [PubMed: 16481914]
105. Flacke S, Fischer S, Scott MJ, et al. Novel MRI contrast agent for molecular imaging of fibrin: implications for detecting vulnerable plaques. Circulation. 2001; 104:1280–1285. [PubMed: 11551880]
106. Yu X, Song S-K, Chen J, et al. High-resolution MRI characterization of human thrombus using a novel fibrin-targeted paramagnetic nanoparticle contrast agent. Magn Reson Med. 2000; 44:867–872. [PubMed: 11108623]
107. Myerson JW, He L, Lanza GM, Tollefsen DM, Wickline SA. Bivalirudin Nanoparticles Enable Simultaneous Detection and Potent Inhibition of Acute Clotting. Circulation. 2011; 124:A15949.
108. Lanza GM, Abendschein DR, Hall CS, et al. In vivo molecular imaging of stretch-induced tissue factor in carotid arteries with ligand-targeted nanoparticles. J Am Soc Echocardiogr. 2000; 13(6): 608–614. [PubMed: 10849515]
109. Lanza GM, Abendschein DR, Hall CH, et al. Molecular imaging of stretch-induced tissue factor expression in carotid arteries with intravascular ultrasound. Invest Radiol. 2000; 35:227–234. [PubMed: 10764091]
110. Lanza GM, Abendschein DR, Hall CS, et al. In vivo molecular imaging of tissue factor in carotid arteries with a one-step ligand conjugated acoustic nanoparticle. Circulation. 1999; 100(18):367.
111. Morawski AM, Winter PM, Caruthers SD, et al. "Magnetic resonance immunocytochemistry": Characterization of "Tissue factor" expression by smooth muscle cells with targeted paramagnetic nanoparticles. Circulation. 2003; 108(17):139–139.
112. Ahrens ET, Young WB, Xu H, Pusateri LK. Rapid quantification of inflammation in tissue samples using perfluorocarbon emulsion and fluorine-19 nuclear magnetic resonance. Biotechniques. 2011; 50(4):229–234. [PubMed: 21548906]
113. Kadayakkara DK, Janjic JM, Pusateri LK, Young WB, Ahrens ET. In vivo observation of intracellular oximetry in perfluorocarbon-labeled glioma cells and chemotherapeutic response in the CNS using fluorine-19 MRI. Magn Reson Med. 2010; 64(5):1252–1259. [PubMed: 20860007]
114. Srinivas M, Morel PA, Ernst LA, Laidlaw DH, Ahrens ET. Fluorine-19 MRI for visualization and quantification of cell migration in a diabetes model. Magn Reson Med. 2007; 58(4):725–734. [PubMed: 17899609]
115. Neubauer AM, Sim H, Winter PM, et al. Nanoparticle pharmacokinetic profiling in vivo using magnetic resonance imaging. Magnetic Resonance in Medicine. 2008; 60(6):1353–1361. [PubMed: 19025903]
116. Pan H, Soman NR, Schlesinger PH, Lanza GM, Wickline SA. Cytolytic peptide nanoparticles ('NanoBees') for cancer therapy. Wiley Interdiscip Rev Nanomed Nanobiotechnol. 2011; 3(3): 318–327. [PubMed: 21225660]
117. Pan H, Marsh JN, Christenson ET, et al. Postformulation peptide drug loading of nanostructures. Methods Enzymol. 2012; 508:17–39. [PubMed: 22449919]
118. Pan H, Myerson JW, Ivashyna O, et al. Lipid membrane editing with peptide cargo linkers in cells and synthetic nanostructures. FASEB J. 2010; 24:2928–2937. [PubMed: 20335225]
119. Evans RG, Leong CL, Anderson WP, O'Connor PM. Don't be so BOLD: potential limitations in the use of BOLD MRI for studies of renal oxygenation. Kidney Int. 2007; 71(12):1327–1328. author reply 1328. [PubMed: 17554358]
120. Winter PM, Neubauer AM, Caruthers SD, et al. Endothelial alpha(v)beta3 integrin-targeted fumagillin nanoparticles inhibit angiogenesis in atherosclerosis. Arterioscler Thromb Vasc Biol. 2006; 26(9):2103–2109. [PubMed: 16825592]

121. Myerson J, He L, Lanza G, Tollefsen D, Wickline S. Thrombin-inhibiting perfluorocarbon nanoparticles provide a novel strategy for the treatment and magnetic resonance imaging of acute thrombosis. J Thromb Haemost. 2011; 9(7):1292–1300. [PubMed: 21605330]
122. Marsh JN, Hu G, Scott MJ, et al. A fibrin-specific thrombolytic nanomedicine approach to acute ischemic stroke. Nanomedicine (Lond). 2011; 6(4):605–615. [PubMed: 21506686]
123. Winter PM, Caruthers SD, Zhang H, et al. Antiangiogenic synergism of integrin-targeted fumagillin nanoparticles and atorvastatin in atherosclerosis. JACC Cardiovasc Imaging. 2008; 1(5):624–634. [PubMed: 19356492]
124. Pan D, Sanyal N, Schmieder AH, et al. Antiangiogenic nanotherapy with lipase-labile Sn-2 fumagillin prodrug. Nanomedicine (Lond). 2012; 7(10):1507–1519. [PubMed: 22709347]
125. Schmieder AH, Caruthers SD, Zhang H, et al. Three-dimensional MR mapping of angiogenesis with alpha5beta1(alpha nu beta3)-targeted theranostic nanoparticles in the MDA-MB-435 xenograft mouse model. FASEB J. 2008; 22(12):4179–4189. [PubMed: 18697838]
126. Zhou HF, Chan HW, Wickline SA, Lanza GM, Pham CT. Alphavbeta3-targeted nanotherapy suppresses inflammatory arthritis in mice. FASEB J. 2009; 23(9):2978–2985. [PubMed: 19376816]
127. Zhou HF, Hu G, Wickline SA, Lanza GM, Pham CT. Synergistic effect of antiangiogenic nanotherapy combined with methotrexate in the treatment of experimental inflammatory arthritis. Nanomedicine (Lond). 2010; 5(7):1065–1074. [PubMed: 20874021]
128. Zhou HF, Yan H, Senpan A, et al. Suppression of inflammation in a mouse model of rheumatoid arthritis using targeted lipase-labile fumagillin prodrug nanoparticles. Biomaterials. 2012; 33(33):8632–8640. [PubMed: 22922023]
129. Cyrus T, Zhang H, Allen JS, et al. Intramural delivery of rapamycin with alphavbeta3-targeted paramagnetic nanoparticles inhibits stenosis after balloon injury. Arterioscler Thromb Vasc Biol. 2008; 28(5):820–826. [PubMed: 18292395]
130. Li AJ, Bibee K, Marsh JN, Weihl CC, Wickline SA. Mdx mice have a defect in autophagy that is restored by rapamycin-loaded nanoparticle treatment. Conference Proceedings of Experimental Biology. 2012
131. Lanza GM, Yu X, Winter PM, et al. Targeted antiproliferative drug delivery to vascular smooth muscle cells with a magnetic resonance imaging nanoparticle contrast agent: implications for rational therapy of restenosis. Circulation. 2002; 106(22):2842–2847. [PubMed: 12451012]
132. Pan H, Ivashyna O, Sinha B, et al. Post-formulation peptide drug loading of nanostructures for metered control of NF-kappaB signaling. Biomaterials. 2011; 32(1):231–238. [PubMed: 20864161]
133. Soman NR, Baldwin SL, Hu G, et al. Molecularly targeted nanocarriers deliver the cytolytic peptide melittin specifically to tumor cells in mice, reducing tumor growth. J Clin Invest. 2009; 119(9):2830–2842. [PubMed: 19726870]
134. Kaneda MM, Sasaki Y, Lanza GM, Milbrandt J, Wickline SA. Mechanisms of nucleotide trafficking during siRNA delivery to endothelial cells using perfluorocarbon nanoemulsions. Biomaterials. 2010; 31(11):3079–3086. [PubMed: 20092889]

Clinical Summary

- Perfluorocarbon nanoparticles (PFC NP) are a non-nephrotoxic molecular imaging agent for noninvasive quantitative assessment of kidney function and injury.
- Functionalized PFC NP allow site-targeted drug delivery as a novel therapeutic modality for treating acute and chronic kidney diseases.

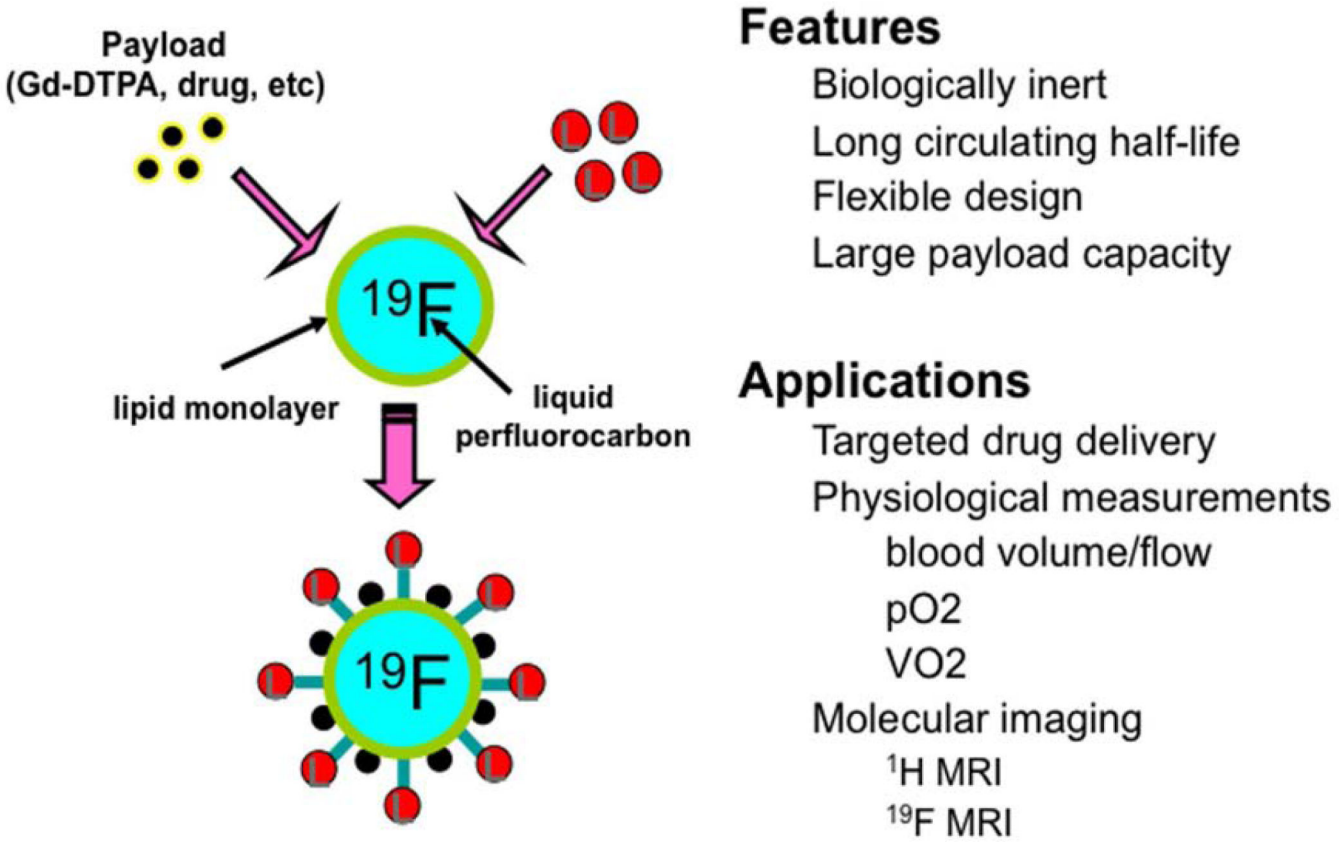

Figure 1.
Paradigm for physiological and molecular imaging with perfluorocarbon nanoemulsions. Reprinted from Wickline et al.[20] with permission.

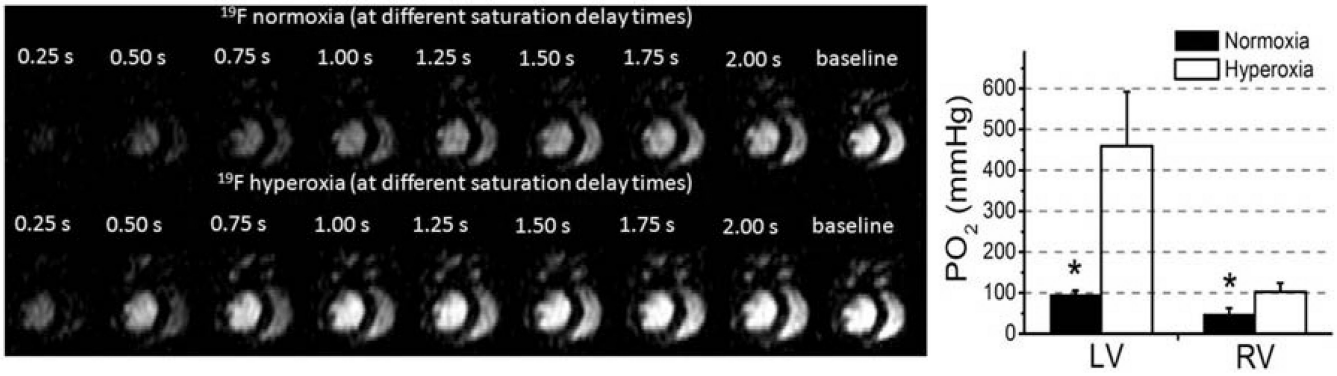

Figure 2.

Left^{19}F BESR images of the mouse heart under hyperoxia and normoxia illustrating signal due to 19F PFC NP that is responsive to blood pO2. **Right**: Measured blood pO_2 based on measured ^{19}F T1 of PFC NP showed pO_2 difference between LV and RV, and between normoxic and hyperoxic conditions for each ventricle. Reprinted from Hu et al. [74] with permission.

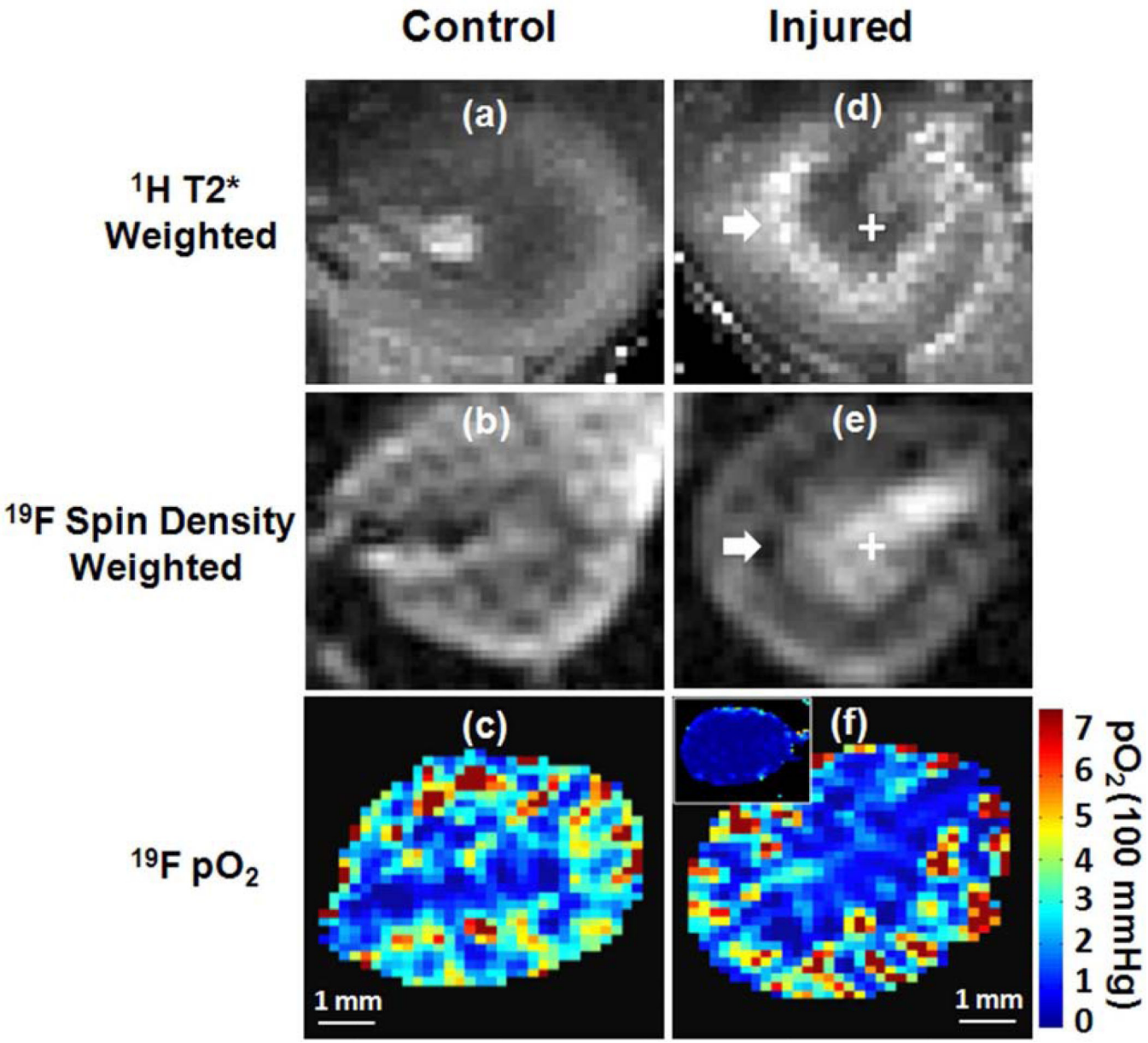

Figure 3.

Representative ^{1}H BOLD T2*-weighted image, ^{19}F spin density weighted image and ^{19}F T1-mapping derived pO_2 map in the left control (**A–C**) and right injured (**D–F**) kidneys of the same mouse. The inserted panel in (**F**) shows ^{19}F MRI detected pO_2 map of another mouse kidney during ischemia. White arrow points to the CM junction of the injured kidney where abnormally increased ^{1}H T2* and decreased ^{19}F signal intensity were detected. Reprinted from Hu et al.[77] with permission.

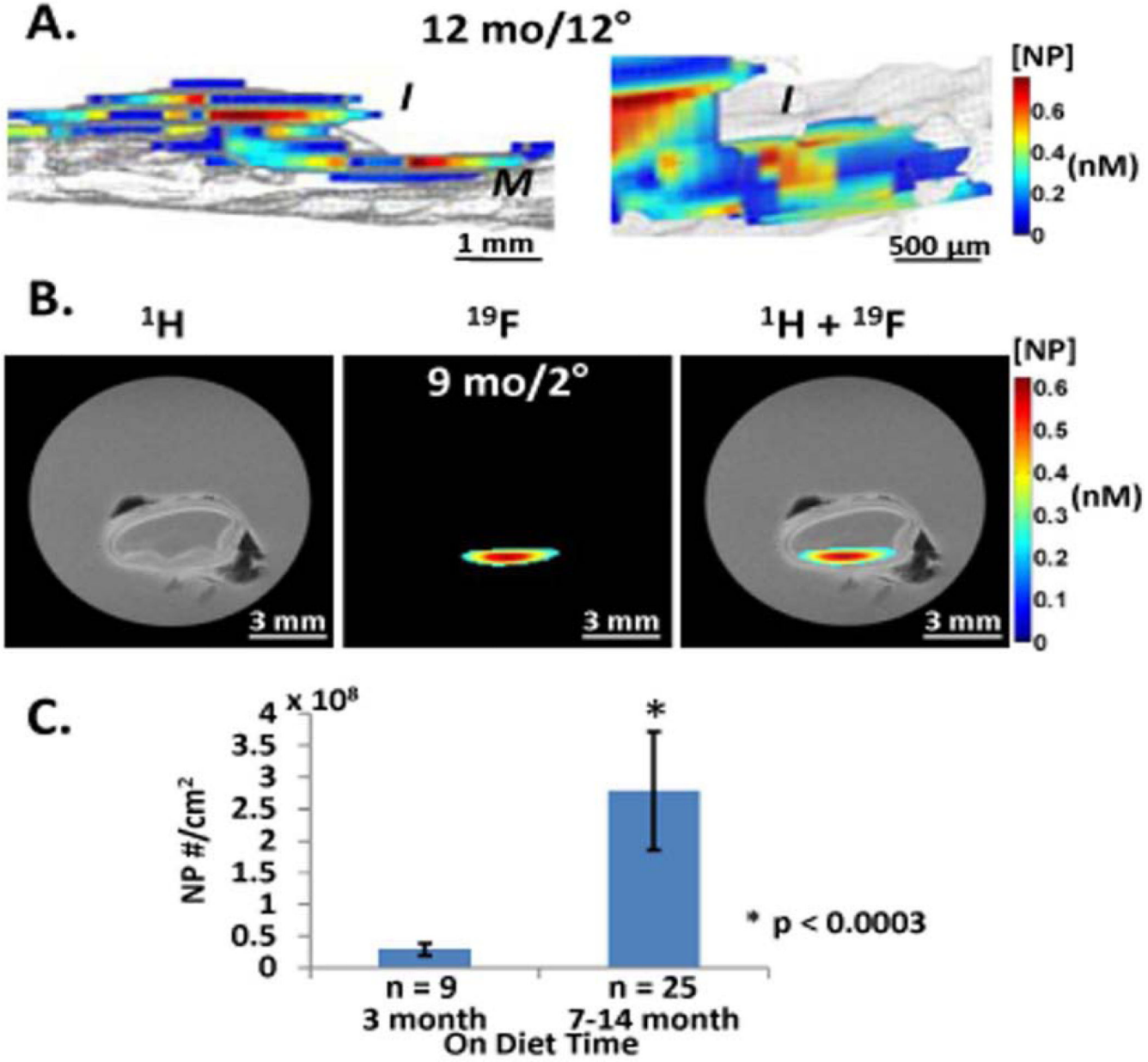

Figure 4.

MRI imaging and quantification of NP signal in cholesterol plaques **(A) Left:** 3D saggital rendering of nanoparticle signals from aorta of 12 mo cholesterol fed rabbit after 12 hours circulation time *in vivo*. ^{19}F MR image registering nanoparticle fluorine cores (color) overlaid on ^{1}H MR image (gray) of aorta show intimal (I) location of particles trapped in thickened plaque (color) atop the medial (M) layer (gray). Particle concentration per voxel is coded in nM (scale bar). **Right:** Close up of intimal layer. (**B**) ^{1}H, ^{19}F and overlay MR transverse images of aortic rings with nanoparticles trapped in intima of thickened plaque from 9 mo cholesterol fed rabbit after 2 hour circulation *in vivo*. Black artifacts are small air bubbles. Note lack of ^{19}F signal from more normal adjacent tissue sections. (**C**) Comparison of normalized CE NP number to the endothelial surface area between 3 month diet and >7

month diet rabbit aorta samples showing 10 fold greater accumulation in older plaques. Reprinted from Zhang et al. [56] with permission.

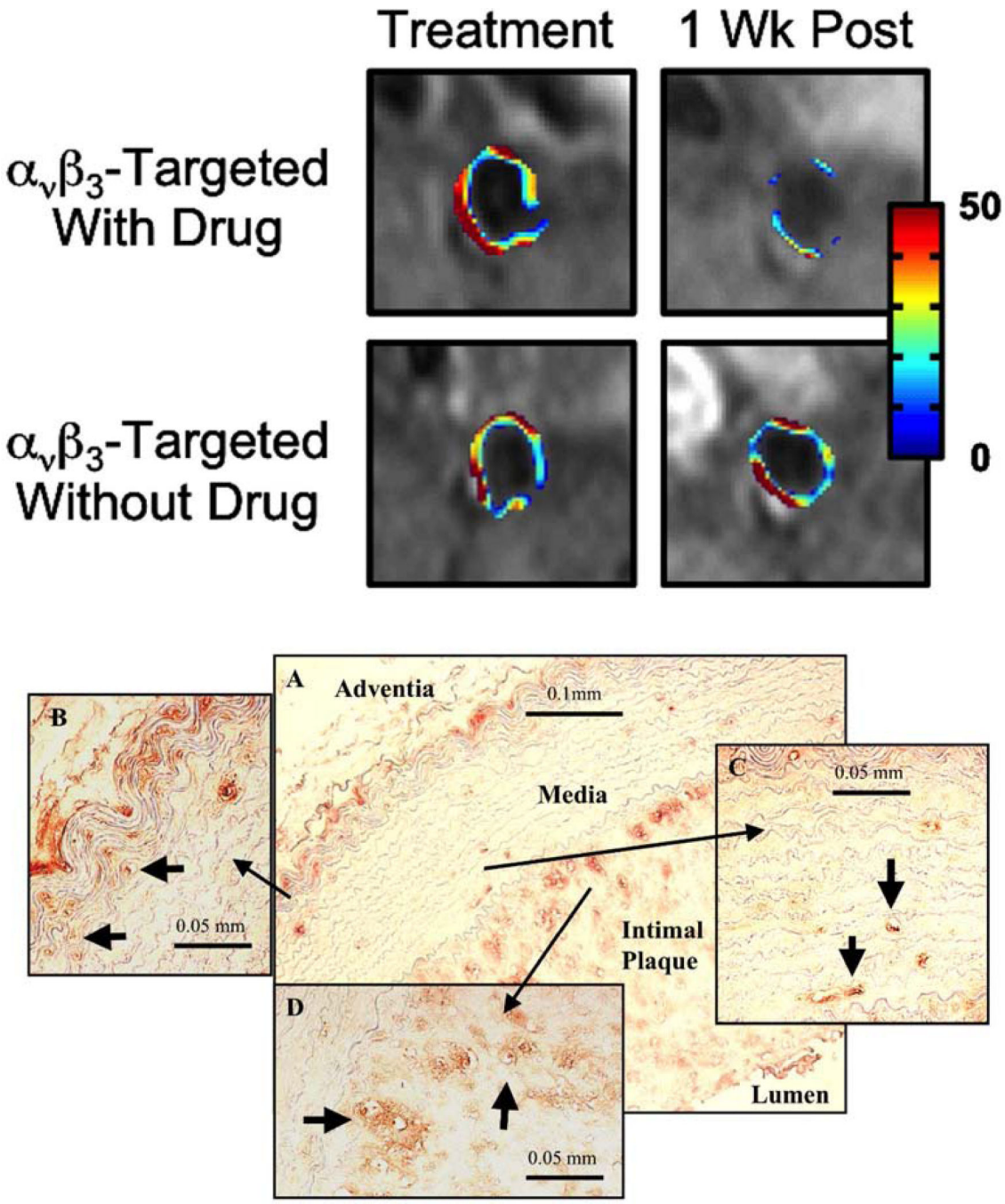

Figure 5.

Top Panel: MRI of neovasculature in rabbit plaque with $\alpha_v\beta_3$-targeted nanoparticles. Significantly lower angiogenesis one week after treatment with targeted fumagillin particles. Rabbits treated with non-targeted fumagillin nanoparticles show high levels of angiogenesis one week post treatment, similar to particles without fumagillin. **Bottom Panel:** Angiogenesis in rabbit atherosclerotic plaque. (**A**) Histological section of abdominal aorta from control animal demonstrating intimal plaque and strong staining for $\alpha_v\beta_3$-integrin (LM-609) at the media-adventia and media-intima interfaces. Angiogenic vessels (arrows)

are observed in the vasa vasorum (**B**), media (**C**) and intimal plaque (**D**). Reprinted from Winter et al. [120] with permission.

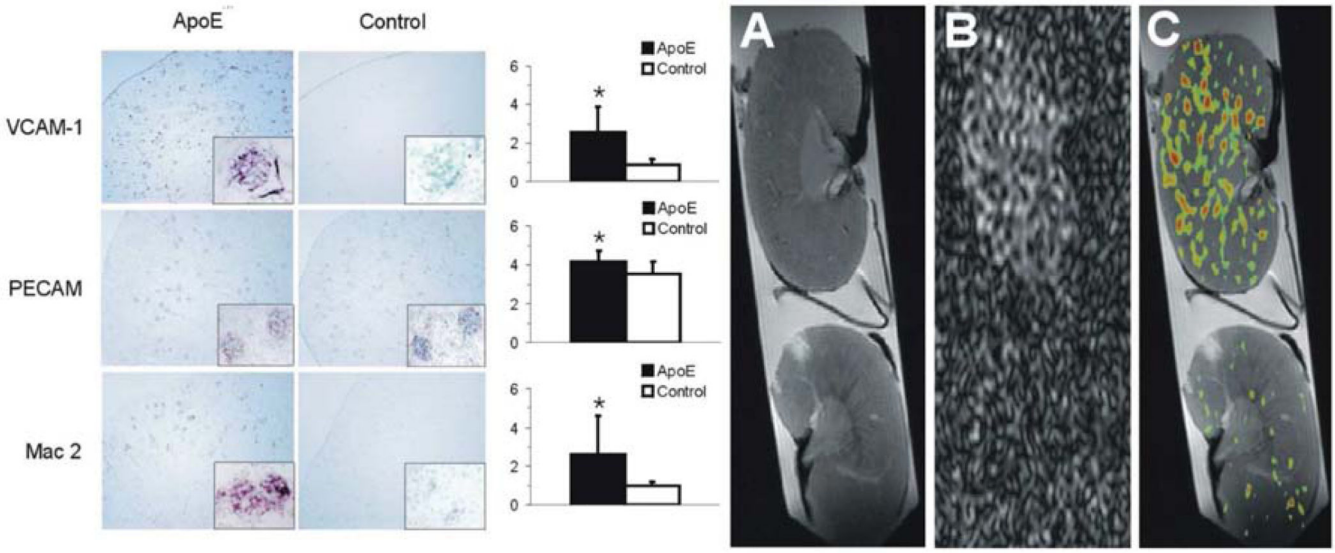

Figure 6.

The ApoE$^{-/-}$ kidney is characterised by significant up-regulation of VCAM-1 expression and a marked infiltration of macrophages into the glomeruli. A representative ^{1}H MR image (**A**) showing structural detail, ^{19}F MR image (**B**), and a composite ^{1}H/^{19}F image (**C**) showing VCAM-1-targeted nanoparticle accumulation in atherosclerotic ApoE$^{-/-}$ (top) and wild-type control (bottom) kidneys, imaged at 12T. Voxels with a signal intensity greater than twice the standard deviation were defined as positive for ^{19}F to produce a distribution map of ^{19}F throughout each kidney, which corresponds to nanoparticle binding via VCAM targeting. Data represent mean (n=6±SD). *represents $p<0.05$. Reprinted from Southworth et al.[101] with permission.

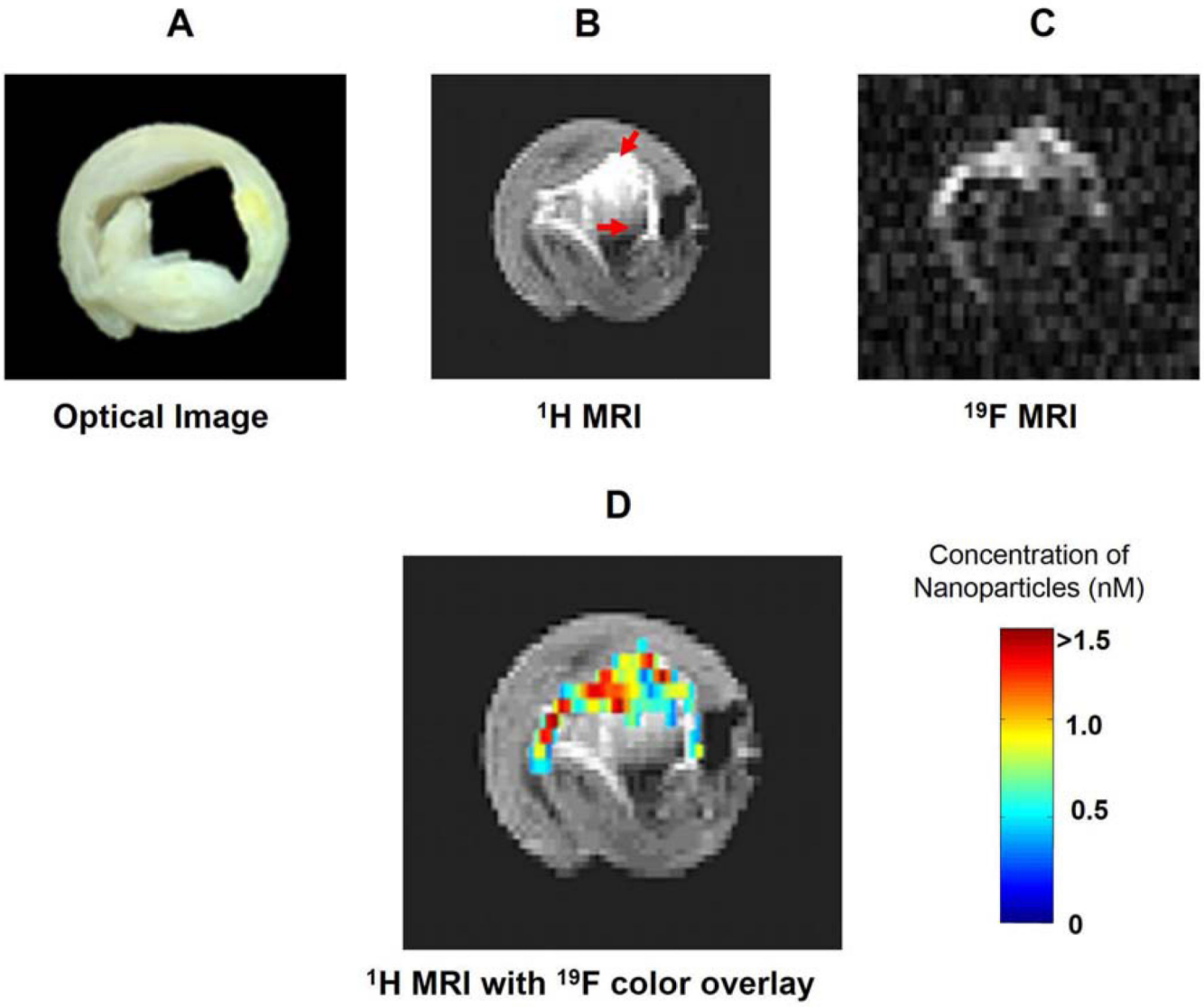

Figure 7.

Fibrin targeted PFC NP binding to human carotid endarterectomy specimen in vitro. (**A**) Optical image of a 5 mm cross-section of a human carotid endarterectomy sample. This section showed moderate lumenal narrowing as well as several atherosclerotic lesions and areas of calcification. (**B**) A ^{1}H image acquired at 4.7 T at the same location shows signal enhancement due to the presence of gadolinium on the targeted particles (red arrows). (**C**) A ^{19}F projection image acquired at 4.7 T through the entire carotid artery sample shows high signal in the same areas due to nanoparticles bound to fibrin. (**D**) ^{1}H image in **B** with a false color overlay of the quantified nanoparticle concentration in the carotid as derived from the ^{19}F image. Reprinted from Morawski et al.[33] with permission.

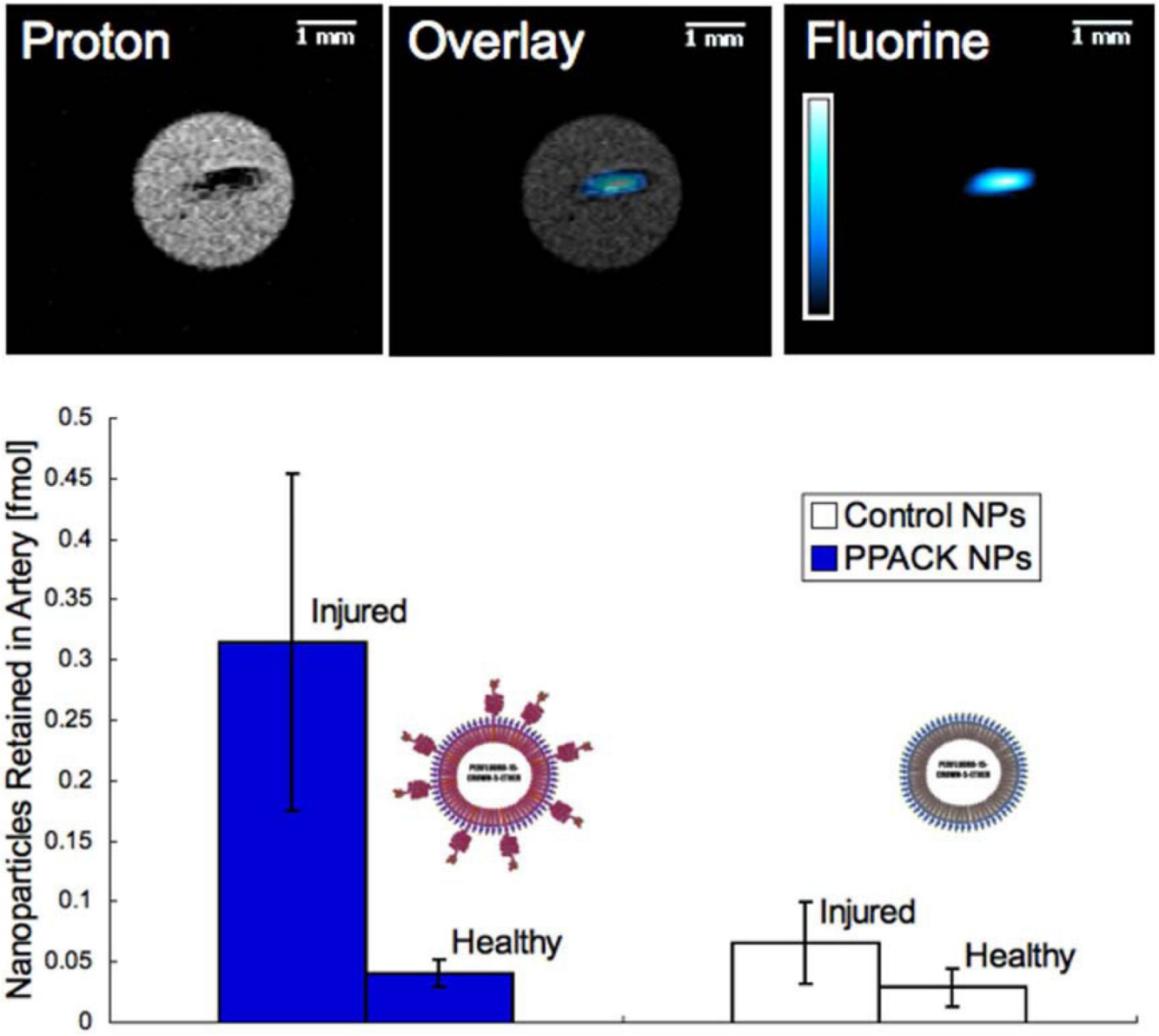

Figure 8.

In mice receiving treatment with control nanoparticles (n=3) or PPACK nanoparticles (n=3), both carotid arteries were excised following induction of occlusive thrombi in the right carotid artery. (**A**) ^{19}F MRI at 11.7T exhibited coregistration of ^{19}F signal from PPACK nanoparticles with ^{1}H images depicting the occlusive clot in the artery. ^{19}F MRS was used to quantify retention of nanoparticles in the injured right carotid artery (RA) and the unharmed left carotid artery (LA) for the two tested nanoparticle treatments. (**B**) Retained are represented in particles mean ± standard error. Reprinted from Myerson et al.[121] with permission.

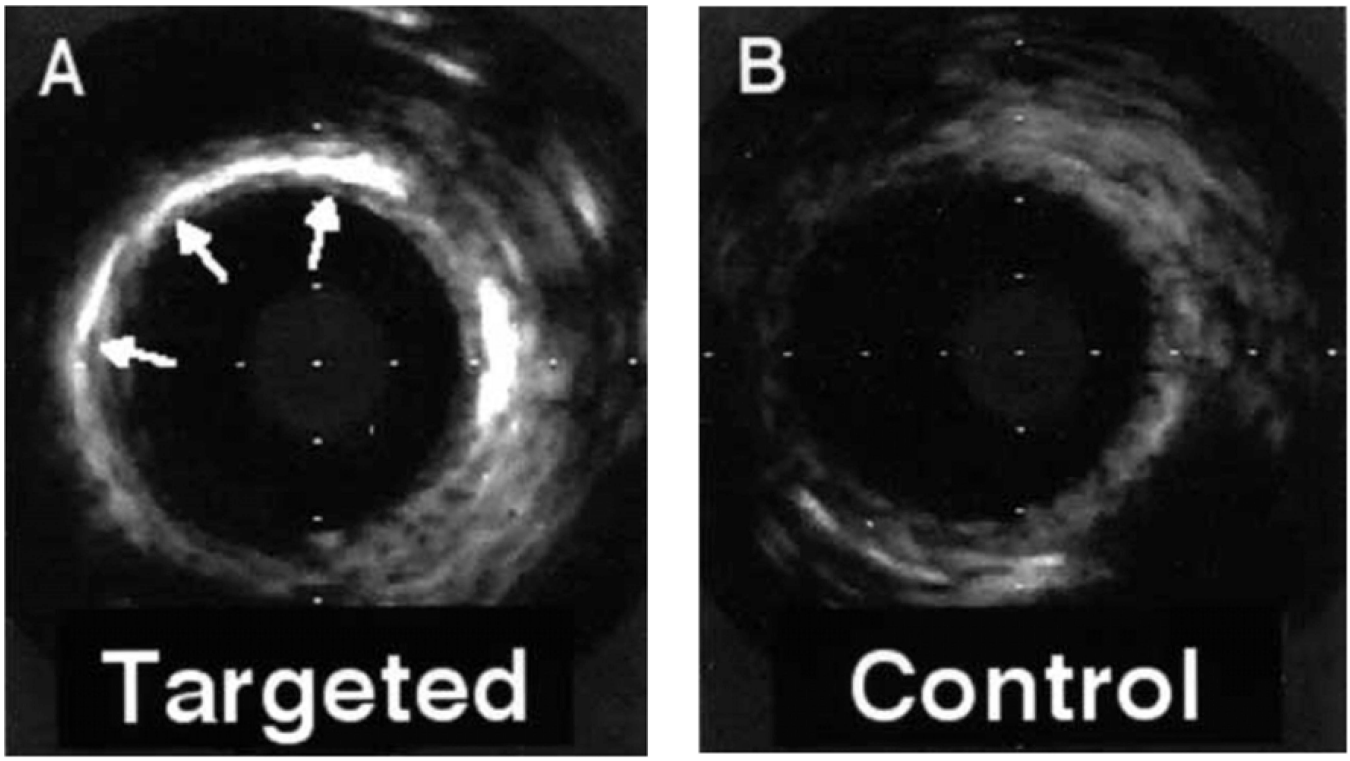

Figure 9.

High-frequency intravascular ultrasonic images of carotid arteries exposed to tissue factor–targeted or control emulsion nanoparticles after angioplasty. (**A**) Bright acoustic enhancement (arrows) in a portion of the vessel wall consistent with nonuniform overstretch injury with the balloon. (**B**) Lack of acoustic enhancement in the vessel wall after control contrast. Similar results were observed in each of 3 animals. Reprinted from Lanza et al.[108] with permission.

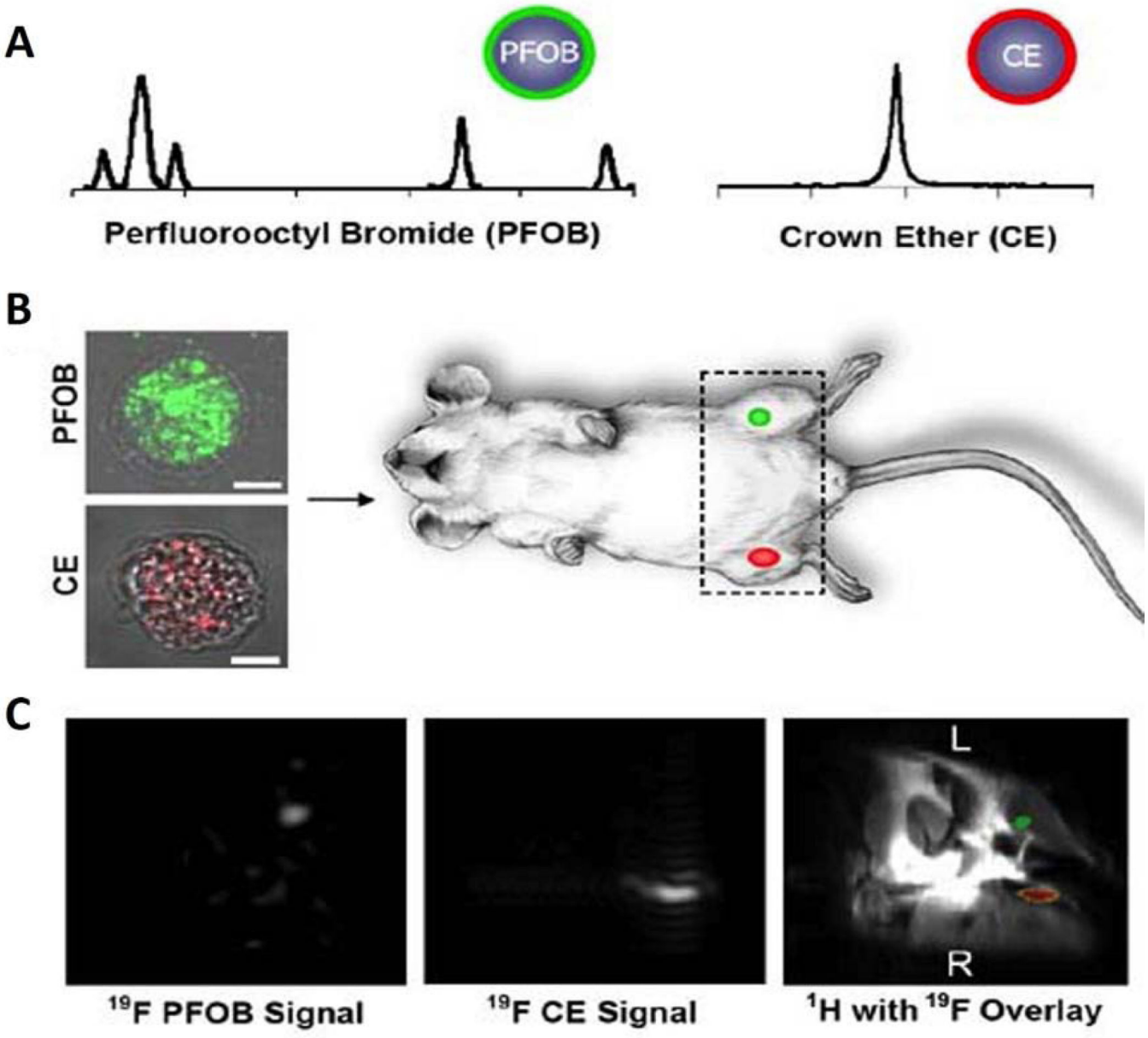

Figure 10.

(**A**) The different ^{19}F spectrospic features between PFOB and CE allows selective detection of PFOB or CE NP labeled cells. (**B**) To determine the feasibility of detecting cells at specific tissue sites after local delivery, one million cells (2×10^4/μL) loaded with CE or PFOB NP were injected into mouse thigh skeletal muscle. At 11.7T, the PFC labeled cells were imaged rapidly in approximately 4 minutes by selectively tuning to PFOB or CE. (**C**) Overlaying the fluorine images atop a conventional matched proton image reveals the ^{19}F PFOB and CE signals are located in the left and right mouse thigh, respectively. Reprinted from Partlow et al. [49] with permission.

Table 1

The application of therapeutic PFC NP in various diseases

Therapeutic Agent	Application	Molecular Target	Reference
PPACK (phenyalanine-proline-arginine-chloromethylketone	anti-thrombosis	thrombin	121
Bivalirudin	anti-thrombosis	thrombin	107
Urokinase	thrombolysis	fibrin	122
Fumagillin	anti-angiogenesis in atherosclerosis	Endothelial aminopeptidase	120, 123
Fumagillin	anti-angiogenesis in cancer	Endothelial aminopeptidase	95, 124, 125
Fumagillin	anti-angiogenesis in arthritis	Endothelial aminopeptidase	126–128
Rapamycin	Restenosis prevention, anti-inflammatory	mTOR	129
Rapamycin	Muscular dystrophy	Autophagy enhancer (via mTOR)	130
Paclitaxel/Doxorubicin	Vascular inflammation, smooth muscle cell inhibition	Tissue Factor	131
Anti NFκB peptides (NBD)	Inflammation, cancer	NFκB (p65)	132
Melittin peptides	cancer	Cell lipid membrane disruptor	116, 133
siRNA	various	mRNA	134